scientific reports

OPEN

Green synthesis of magnesium oxide nanoparticles using *Hyphaene thebaica* extract and their photocatalytic activities

Abdul Muhaymin[1,2,3], Hamza Elsayed Ahmed Mohamed[1,2]✉, Khaoula Hkiri[1,2], Ammara Safdar[1,2,3], Shohreh Azizi[1,2] & Malik Maaza[1,2]

Magnesium oxide nanoparticles (MgO NPs) represent an interesting inorganic material widely utilized across various fields including sensing, antimicrobial applications, optical coatings, water purification, fuel additives, absorbents, and catalysis, owing to their exceptional broad energy band gap, surface affinity, and strong chemical and thermal durability. In this investigation, MgO NPs were successfully synthesized through a green approach employing fruit extract from the gingerbread tree (Hyphaene thebaica). Analysis via scanning electron microscopy (SEM) and transmission electron microscopy (TEM) confirmed their agglomerated quasi-spherical shape with a size range of 20–60 nm. The X-ray diffraction (XRD) pattern exhibited prominent peaks at planes (200) and (220), indicating the high crystallinity of MgO NPs with a crystallite size of 32.6 ± 5 nm while Energy-dispersive X-ray spectroscopy (EDS) analysis highlighted the composition comprises 40.47% Magnesium and 48.64% Oxygen by weight. Fourier transform infrared spectroscopy (FT-IR) revealed characteristic Mg-O bonds through peaks at 560 cm^{-1} and 866 cm^{-1}, while Raman spectroscopy affirmed the cubic structure of MgO. Subsequently, the photocatalytic performance of MgO NPs under visible light irradiation was evaluated. Remarkably, the addition of 1 g/L of MgO nano-catalyst resulted in a degradation efficiency of 98% after 110 min on methylene blue dye, showcasing the high catalytic activity of MgO NPs. This remarkable photocatalytic efficiency emphasizes the potential of MgO NPs in environmental remediation.

During recent decades, nanoparticles (NPs) have captured significant interest because of their unique characteristics such as biocompatibility, superior mechanical performance, thermal and chemical stability, high strength, and damping[1]. Among all, metal and metal oxide NPs have high surface area to volume ratio and smaller crystalline sizes used in a broad range of fields, including optical, magnetic, sensing, and electronics[2,3]. As a result, several metal oxide NPs are developed, including $CoFe_2O_4$, Fe_3O_4, MgO, TiO_2, and, ZnO for a variety of applications[4–7].

Magnesium oxide nanoparticles (MgO NPs) are being widely researched among metal oxide NPs due to their high biocompatibility, excellent surface reactivity, broad band gap, and good stability[8,9]. They have been used in paints, medicines, electronics, ceramics, additives, catalysis, and photochemical products[10,11]. Additionally, MgO nanoparticles are capable of absorbing X-rays and visible light, ultraviolet radiation due to their wide band gap energy, which typically ranges from 3.18 to 4.85 eV[12,13]. Magnesite ore, containing 43.32% MgO, is readily available as a raw material in the Eastern Desert of Egypt and is mined at a low cost. The production cost of MgO nanoparticles is lower compared to many other metal oxide nanoparticles, offering significant economic advantages over other photocatalysts and even modified adsorbents. The structure of MgO nanoparticles demonstrates a high efficiency in removing various pollutants, which can be attributed to their high surface-to-volume ratio that enhances surface reactions[14]. Moreover, MgO nanoparticles and their composites have shown promise as effective adsorbents and photocatalysts for the removal of pollutants from industrial wastewater[15–17].

[1]College of Graduate Studies, UNESCO-UNISA Africa Chair in Nanosciences-Nanotechnology, University of South Africa, Muckleneuk Ridge, P.O. Box 392, Pretoria, South Africa. [2]Material Research Department (MRD), Nanosciences African Network (NANOAFNET), iThemba LABS-National Research Foundation, 1 Old Faure Road, Somerset West, PO Box 722, Somerset West 7129, Western Cape, South Africa. [3]Preston Institute of Nanoscience and Technology, Preston University Kohat, Islamabad Campus, Islamabad, Pakistan. ✉email: hamza@aims.ac.za

Various methods are developed to synthesize MgO NPs, such as hydrothermal, spray pyrolysis, microwave, sonochemical, co-precipitation, and sol–gel method[18–21]. These conventional preparation methods have drawbacks, including the requirement of toxic chemicals, high amounts of external heat, and containing side products that can be biologically and environmentally hazardous. Therefore, there is always a need to develop environmentally friendly, economical, energy-efficient biochemical procedures to evade the toxicity of chemicals in the fabrication of NPs[22–25]. To avoid these complications, natural organisms (plants, bacteria, marine algae, and sponges) provide alternative resources to biosynthesize the metal and metal oxide NPs[26–28]. These plants contain different biomolecules, i.e., flavonoids, alkaloids, terpenoids, and carboxylic acids that can serve as a chelating and reducing agent as well as stabilize the formation of metal oxide NPs[29]. The biosynthesis of MgO NPs with plant extract is also a simple process with safety, less toxicity, and an environment-friendly nature[30]. Table 1, provides a literature review on various preparation techniques and the surface morphology of MgO NPs[31–36].

Hyphaene thebaica, locally known as Doum (Arabic) and gingerbread tree (English), belongs to the family Arecaceae. In history, H. thebaica has been widely used as a medicine for hypertension, bleeding, lowering blood pressure, dyslipidemia, and hematuria, as a diaphoretic and diuretic[31]. Successful green synthesis of different metal and metal oxide NPs through H.thebaica has been reported in recent years[32–36]. Mohamed et al. synthesized Ag NPs through an aqueous extract of H. thebaica. The biological and physiochemical properties were studied through SEM, TEM, XRD, UV–Vis, FTIR, and *in-vitro* biological assays[37]. The results showed excellent biological activities of AgNPs in the size range of 5–70 nm, and anisotropic behavior was observed with different morphologies.

This study focuses on the biosynthesis of MgO NPs using the extract of Hyphaene thebaica and examines their photocatalytic behavior. The physicochemical properties of the nanoparticles were characterized using a range of techniques, including SEM, TEM, XRD, EDX, FTIR, and Raman spectroscopy. Additionally, the photocatalytic efficiency of the MgO NPs was evaluated by investigating their ability to degrade methylene blue (MB) dye under specific conditions. The significance of this work lies in the synthesis process of MgO NPs, which have several significant advantages. It employs water as the sole universal solvent, eliminating the need for additional base or acid chemicals for pH control. This process does not require any supplementary catalysts, relying solely on the natural extract of H.thebaica as an effective chelating agent facilitated by its phytochemicals and enzymatic compounds. Moreover, the synthesis is conducted at room temperature and under atmospheric pressure, further simplifying the procedure. There is no necessity for extra thermal annealing, and the method consistently produces nano-scaled particles, underscoring the efficiency and practicality of this environmentally friendly approach.

Materials

$Mg(NO_3)_2.6H_2O$ (> 98%) was obtained from Sigma Aldrich and used without further purification. Hyphaene thebaica was sourced from the local market in Aswan, Egypt. Deionized water with a conductivity lower than 10^{-6} Scm^{-1} was employed in the experimental procedures.

Plant extract preparations

Organic Hyphaene thebaica fruits were obtained from the city of Aswan, Egypt. To remove any pollutants, the fruit was washed with distilled water and shade-dried. Then, the dried fruits were ground to powder and 5 g of powder was added to 100 ml distilled water under 70–90 °C for 2 h. Then, the extraction solution was allowed to cool at room temperature and filtered thrice for any leftovers using Whatman filter paper. The filtrate was obtained as a yellowish-golden solution and used for further procedure.

Green synthesis of MgO nanoparticles via *Hyphaene* thebaica

6g of $Mg(NO_3)_2.6H_2O$ was added to 100 mL of plant extract solution and stirred. After addition, a color change from darkish yellow to light yellow was observed. After aging overnight, the solution was kept in an oven at 150 °C for 3–4 h until it dried and turned into powder. For annealing, the powder was kept at 500 °C for 2 h and collected for further characterization and photocatalytic application as illustrated in Fig. 1.

Physical characterization

Different techniques were used to evaluate the physical properties of MgO. The shape, surface, and internal morphologies were studied by SEM and TEM images. The size was also measured by processing SEM images through

			Calcination temperature (°C)	References
MgO		Conical, Nanoflowers	500	63
MgO		Nano-flakes		64
MgO		Cubic		
MgO				
MgO				
MgO	Bacteria-mediated synthesis	Cubic	300	65
MgO	Plant mediated synthesis	Cubic	500	Present

Table 1. Comparison of previously reported studies for MgO NPs.

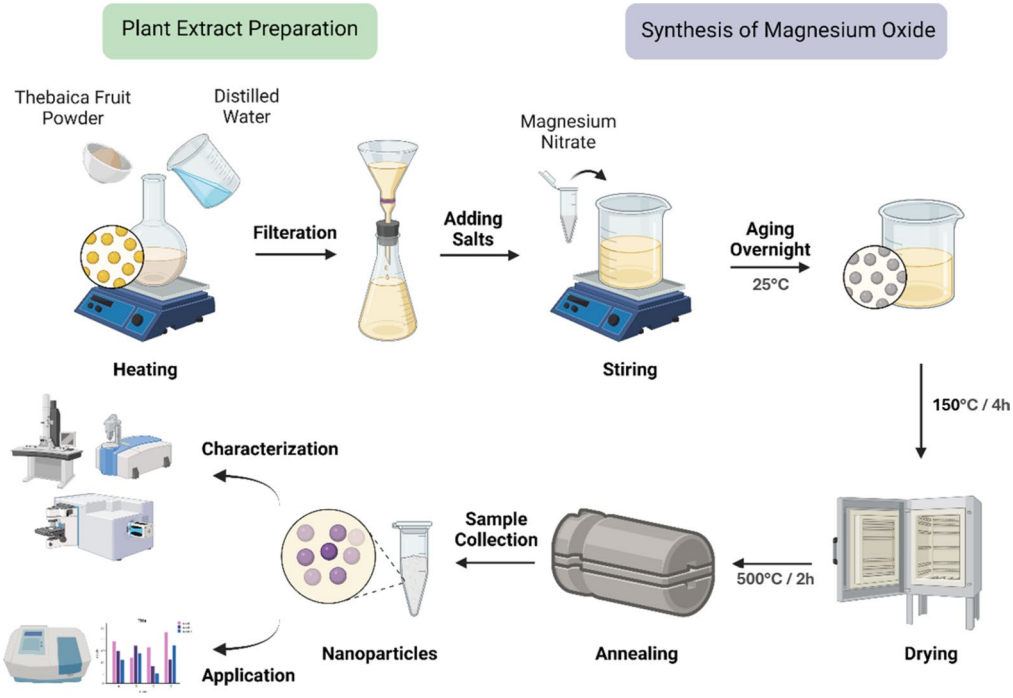

Fig.1. Schematic Diagram of Preparation of Magnesium Oxide NPs.

ImageJ software. XRD was performed using an X-ray diffractometer and the crystal structure was determined with mean crystallite size through Scherer approximation. EDX analysis was used to study the composition. The functional groups and nature of NPs were determined by FTIR and Raman Spectroscopy.

Photocatalytic performance of MgO NPs

The effectiveness of the synthesized MgO nanoparticles was evaluated via catalytic degradation of methylene blue (MB) azo dye under visible light at room temperature. Table 2 shows the chemical characteristics of MB dye. The photocatalytic testing was executed using a steel reaction chamber containing a 125 W lamp positioned centrally. Analysis of the UV–visible absorbance profile of the MB dye revealed a maximum absorption at 665 nm. A solution containing 10 ppm of MB dye was prepared (neutral pH), and 1 g/L of MgO nano-catalyst was added under stirring. Ice was utilized to maintain the temperature within the 25–30 °C range. To establish absorption equilibrium, the solution was maintained in darkness for 30 min before measuring the absorbance values using a UV–Vis spectrometer. Absorbance measurements were taken every 10 min under visible light, and the solution was exposed to light for a total of 110 min. Typically, the degradation of MB dye proceeded according to pseudo-first-order kinetics due to the reason that the concentration of the dye was much lower than that of the catalyst, with the extent of degradation quantified by MB concentration ratio, represented as C_f/C_i. Absorption percentage was computed according to the formula described[38–40]:

$$Percent\ Degradation = \left(C_i - C_f\right)/C_i x\ 100\,\% \tag{1}$$

where C_i and C_f are the initial and final concentrations.

Chemical structure	Dye type	Abbreviation	Chemical formula	λ_{max} (nm)	Molecular weight (g/mol)
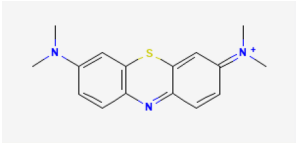	Cationic	MB	$C_{16}H_{18}N_3ClS$	665	319.85

Table 2. Characteristics of Methylene Blue Dye.

Results and discussion

XRD analysis

XRD analysis was performed using the CuKα radiation in the range of 30–80° (2θ). Figure 2 shows the XRD analysis of green synthesized MgO NPs by Hyphaene thebaica fruit extract. The XRD peak contains 36.94°, 42.86°, 62.30°, 74.70°, and 78.62° are corresponding 2θ values that are attributed to (111), (200), (220), (311) and (222) planes of cubic MgO accordingly. Crystal planes resemble the crystal phase of JCPDS Card No. 97–7746. A sharp and intense peak is observed in the XRD spectrum around (200) which prove the high crystallinity of MgO NPs. The average crystalline size was measured by Debye Scherrer's formula (Eq. 1).

$$D = \frac{0.9\lambda}{\beta \cos\theta} \tag{2}$$

where λ is the wavelength of Cu-kα radiation, β is the full-width half-maximum (FWHM) in radians, and θ is the angle of diffraction (in radians). The calculated average crystalline size for the obtained MgO NPs was 30 nm, and the computed lattice constant of MgO NPs is 4.213 Å. Additionally, the subsequent formulas (3) and (4) were employed to calculate the dislocation density δ and lattice strain ε[31].

$$\delta = \frac{n}{D^2} \tag{3}$$

$$\varepsilon = \frac{\beta \cos\theta}{4} \tag{4}$$

The observed δ and ε values for the MgO NPs were 1.11×10^{15} lines/m^2 and 2.35×10^4, respectively. The decrease in crystallinity, indicated by the reduction in crystallite size and the rise in dislocation density, demonstrates the impact of the biosurfactant on the nanoparticles. The increased presence of defects in the MgO NPs likely contributes to their improved catalytic activity. Furthermore, the smaller crystallite size leads to tighter packing, more point contacts, and better inter-particle conductivity, which are expected to enhance the performance of the MgO NPs as a photo-catalytic material.

Microscopic and elemental analysis

The SEM micrographs of MgO confirm the formation of quasi-spherical NPs with agglomeration as shown in (Fig. 3a,b) while HR-TEM confirms the spherical NPs (Fig. 4 A,B,C,D,E, F) with distinct boundaries (Fig. 2). The size of MgO NPs was measured to be in the range of 20–60 nm as calculated with ImageJ software (Fig. 3c). The SAED Pattern (Fig. 4G) of NPs show the regular arrangement of particles in crystal lattice indicating good crystallinity. The cloudy appearance in SEM can be due to the presence of electrostatic interaction between MgO NPs as also reported by Pugazhendhi et al.[41] and also the presence of carbonates on the surface[42]. Hassan et al. reported the spherical shape of MgO NPs prepared by Rhizopus oryzae by studying its morphology with SEM[43]. The morphology of ZnO NPs prepared by H.thebaica was also studied by H.E.A. Mohamed et al. The SEM and TEM images confirm the spherical shape and smaller size of ZnO NPs.

The selected area electron diffraction (SAED) pattern revealed concentric rings accompanied by discrete spots, indicating the polycrystalline nature of the sample, as shown in Fig. 4G. Each ring corresponds to specific crystal planes, facilitating distinct Bragg reflections and lattice spacing. The stippled bands are associated with reflections

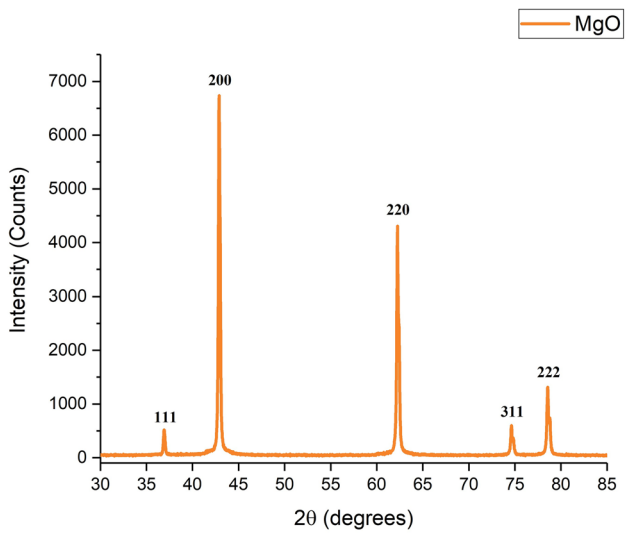

Fig.2. XRD analysis of green synthesized MgO NPs.

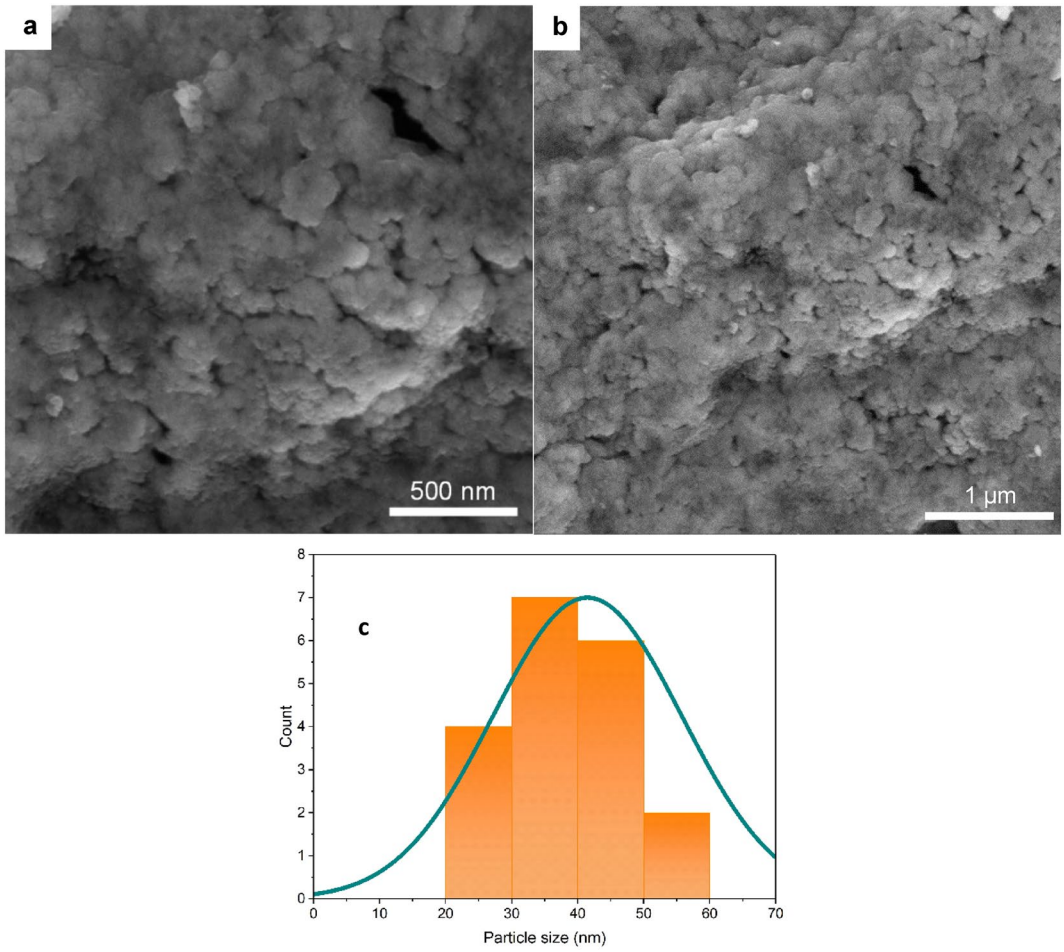

Fig.3. SEM images of green synthesized MgO NPs at different magnifications: (**a**) 100 kx (**b**) 50 kx (c) Histogram depicting particle size distribution derived from the SEM images.

at the (111), (200), (220), and (222) planes within the Fm3m space group. EDX analysis reveals prominent peaks corresponding to Mg and O, providing strong evidence for the formation of MgO (see Fig. 5). The composition comprises 40.47% Mg and 48.64% O by weight. Additionally, minor amounts of other elements such as K and Cl are present, constituting 8.42% and 2.46% respectively. The presence of potassium (K) and chlorine (Cl) can be attributed to the green synthesis method, which incorporates plant extracts or biological materials. These natural sources inherently contain potassium and chlorine, leading to their incorporation into the nanoparticles.

Dobrucka et al. also analyzed the composition of MgO nanoparticles, noting that the presence of peaks between 0.5 and 1.5 keV confirms the successful synthesis of the nanoparticles by using an aqueous extract of Artemisia abrotanum, which aligns with our findings. Their EDX profile of MgO nanoparticles reveals the weight percentages of Mg, O, Al, Si, K, and Ca to be 13.9%, 39.4%, 1.4%, 0.3%, 0.8%, and 0.5%, respectively which indicate minor incorporation of ions from plant extract[44].

Raman spectroscopic analysis

Raman spectroscopy was employed to investigate the phase formation and structural attributes of the synthesized MgO nanoparticles (NPs), within the range of 230 cm^{-1} to 1500 cm^{-1}. The recorded Raman spectrum, depicted in Fig. 6, shows prominent peaks at 280 cm^{-1}, 482 cm^{-1}, 806 cm^{-1}, 980 cm^{-1}, 1054 cm^{-1}, and 1292 cm^{-1}. The peaks observed at 280 cm^{-1}, and 482 cm^{-1} were attributed to the cubic structure of MgO NPs. Previous studies have indicated that MgO reacts with CO_2 to form $MgCO_3$[45–47]. The peak observed at 1054 cm^{-1} can be attributed to the carbonate group (CO_3^{2-}), supporting the surface covering as confirmed via SEM[42]. In MgO microcrystals, Ishikawa et al. demonstrated first-order Raman scattering, noting peaks at 280 cm^{-1}, 446 cm^{-1}, and 1088 cm^{-1} [48]. These peaks are absent in bulk MgO, and the shift in our observed peaks relative to Ishikawa et al. can be attributed to side effects. Akram et al. reported Raman peaks at 268 cm^{-1}, 440 cm^{-1}, and 1339 cm^{-1}, corresponding to the cubic structure of MgO[49]. These peaks indicate our formation of MgO NPs and are attributed to tangential modes in the amorphous phase[50]. Furthermore, other researchers have noted that $Mg(OH)_2$, when subjected to annealing temperatures of 400 °C and above, transforms into MgO. The peaks observed at 280 cm^{-1} and 445 cm^{-1} are occasionally also associated with the bulk phase of $Mg(OH)_2$, indicating the presence of surface contamination in nanoscale MgO[42]. This analysis emphasizes the significant structural transformations and the presence

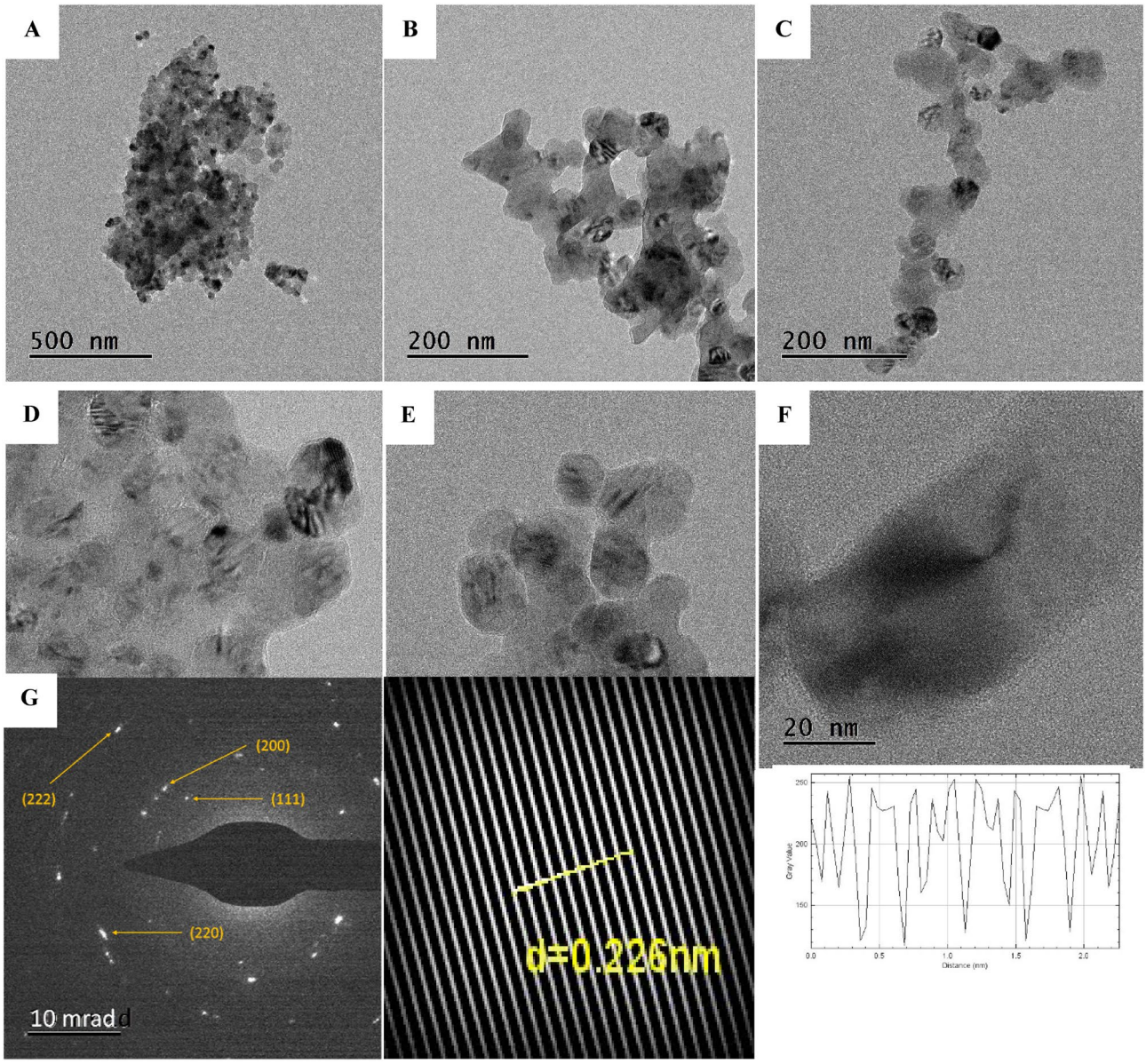

Fig.4. HR-TEM images of MgO NPs at different magnifications (**A**) 500 nm; (**B**) and (**C**) 200 nm; (**D**) and (**E**) 100 nm; (**F**) 20 nm and (**G**) SAED pattern of MgO NPs.

of various phases in the synthesized MgO nanoparticles, providing insights into their formation mechanisms and structural properties.

FTIR spectroscopic analysis

FTIR spectroscopic analysis was conducted to identify the functional groups involved in the chemical reactions during the formation of MgO nanoparticles, as illustrated in Fig. 7. The analysis revealed the presence of C–H (alkanes) rock bonds at 2923 cm^{-1} in the extracts, which transformed into CH_2 bending and C–H "oop" (aromatic) bonds, respectively, during the synthesis of MgO nanoparticles. Mg-O bond was attributed to the intense peak at 560 cm^{-1} as evidenced by literature[51,52].

Additionally, the presence of the MgO was confirmed by the peak at 866 cm^{-1}, which also indicated the occurrence of δ (O–C = O) bonds. This finding suggests that the degradation of alkanes and aromatics took place during the synthesis process, likely due to the utilization of magnesium nitrate as the precursor[19]. These alterations are attributed to changes such as oxidation, reduction, or degradation of phytochemical compounds occurring during the formation of MgO nanoparticles[53]. The FTIR spectral chart also identified the presence of alcohol, phenol, alkynes, and carboxylic acid. The broad absorption peak observed at 3440 cm^{-1} and peak at 1460 cm^{-1} in the prepared sample can be attributed to stretching and bending vibrations of hydroxyl groups (O–H) respectively. The weak absorption band located at 1104 cm^{-1} can be attributed to the stretching vibration of CO_2

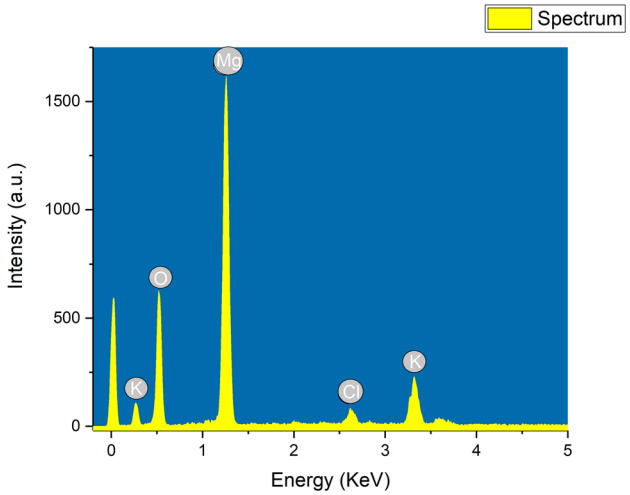

Fig.5. EDS Spectrum of MgO NPs.

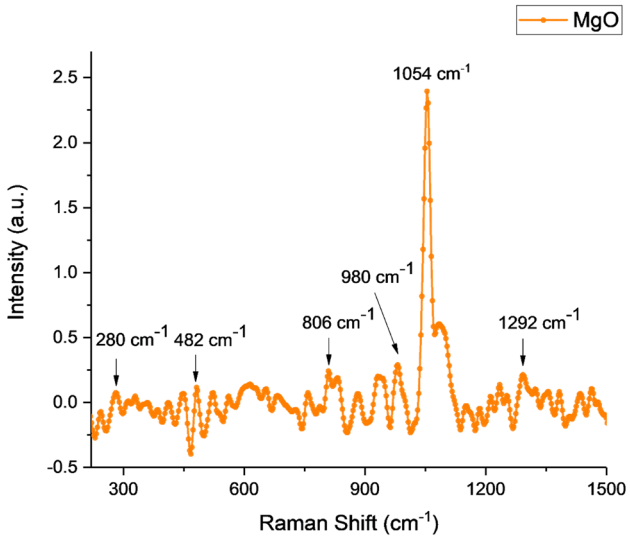

Fig.6. Raman Spectrum of MgO NPs.

molecules or C-O saturated ions. The presence of these functional groups indicates the flavonoids, terpenes, polyphenols, alkaloids, and terpenoids from H. thebaica extract.

Generally, the green synthesis of nanoparticles involves three main stages: activation (involving reduction and nucleation), growth, and termination[54]. The abundance of hydroxyl groups in flavonoids, which possess rich electrons, effectively reduces Mg^{+2} ions during the activation stage. Interaction between hydroxyl groups and Mg ions leads to a conversion of flavonoids from the enol to the keto form, releasing reactive hydrogen atoms that, in turn, reduce Mg ions and form nanoparticles. Nucleation occurs when Mg ions are reduced, resulting in the formation of small nanoparticles. During the growth phase, these nanoparticles aggregate to form various morphologies. Nanoparticles reach their maximum activity during the termination phase, where they attain a stable form and size[55,56]. According to Tamilselvi et al., the detection of the peak within the range of 660–540 cm^{-1} serves as strong evidence for the existence of MgO, aligning with the observations made in our study. Phytochemicals extracted from aqueous sources contain various functional groups, which are integral to the synthesis process of MgO nanoparticles[57].

Photocatalytic studies

The photodegradation of the MB dye using MgO NPs as a catalyst is shown in Fig. 8. The experiments were conducted to determine the catalyst's impact on visible radiation for the degradation of MB dye. Results have shown that in dark conditions, MB dye intensity is at its highest. The MB dye's absorption intensity gradually fades with time. After 110 min, the absorbance value was measured very low, and the solution of MB dye became colorless, indicating pollutant photodegradation under visible radiation[58]. The degradation efficiency was 98% after 110

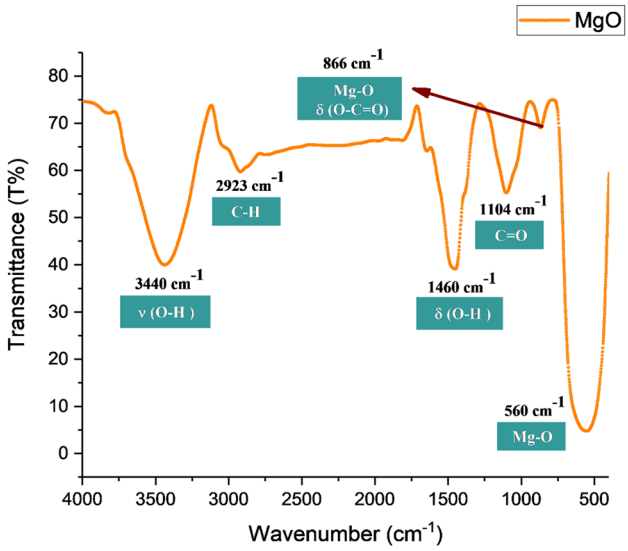

Fig.7. FTIR Spectrum of MgO NPs.

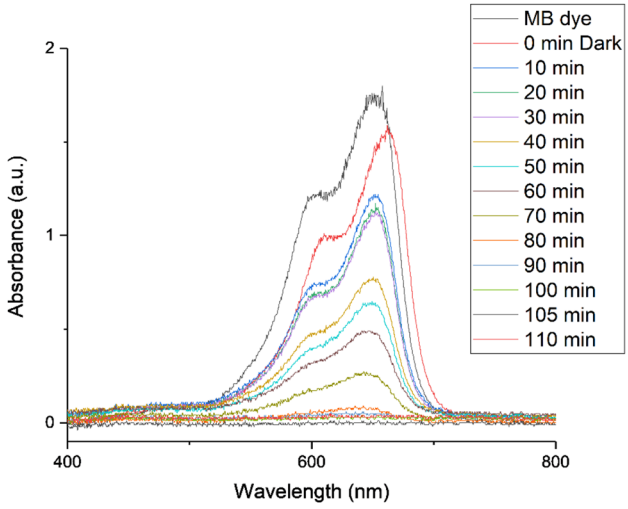

Fig.8. UV–Vis spectra showing the photocatalytic degradation of methylene blue dye using MgO nanoparticles as the nanocatalyst.

Photocatalyst	Synthesis Method	Photodegradation efficiency (%)	References
Hierarchical Cu_2O	Biological	55	66
Cu_2O-rGO	Biological	72	67
CuO-nanozeolite X	Biological	68	68
SnO2	Biological	83	69
ZnS	Biological	23	70
Sr-doped ZnO	Chemical	78.5	71
ZnO	Chemical	37	72
MgO	Biological	98	This study

Table 3. Comparative Photodegradation efficiency of different metal oxide nanoparticles.

min under visible light irradiation. Table 3 indicates that MgO nanostructures exhibit higher photocatalytic activity compared to some other reported metal oxide nanoparticles. The high catalytic activity of MgO NPs can be due to the enhanced surface area and smaller crystallite size. The broadening of the band gap in MgO NPs is likely to enhance their absorption of visible light, thereby significantly increasing the photodegradation rate of methylene blue dye. Similarly, Rawat et al. reported that the wider band gap of biogenic ZnO NPs contributed to a higher catalytic degradation of yellow dye, achieving a rate of 93.38%[59].

Three models have been applied to analyze the experimental data on the photocatalytic degradation of MB by MgO NPs, aiming to elucidate the degradation mechanism. The zero-order kinetic model is expressed by the Eq. (5). Where C_o represents the initial concentration of MB, C_t represents the concentration of MB at time t, and k is the degradation rate coefficient. Figure 9a illustrates a graph of C_t/C_o versus t, displaying a linear relationship with a slope of -k/Co. The linear behavior of the first-order kinetic model is described by the Eq. (6). In Fig. 9b, the value of k is determined from the slope of the linear plot of -Ln(Ct/Co) against time (t). The second-order kinetic model is represented by the Eq. (7):

$$\frac{C_t}{C_o} = 1 - \frac{k_o}{C_o}t \tag{5}$$

$$Ln\frac{C_t}{C_o} = -k_1 t \tag{6}$$

$$\frac{1}{C_t} - \frac{1}{C_o} = k_2 t \tag{7}$$

The slope of the straight line of ($1/C_t$ -$1/C_o$) vs *t* indicates a value of *k*, as shown in Fig. 9c. Upon illumination with photons of the appropriate wavelength, the as-prepared MgO photocatalyst generates electron–hole (e−/h+) pairs. Exposure to visible light excites electrons within the photocatalyst, causing them to transition from the valence band to the conduction band. These energized electrons then interact with the photocatalyst's surface, leading to the formation of superoxide ions (O^{2-}). Through protonation, these superoxide ions generate HOO• radicals, which can further react with electrons to produce H_2O_2. Simultaneously, the positively charged holes (h+) in the valence band react with water, resulting in the generation of H_2O/O

$$MgO + h\upsilon \rightarrow e^-_{CB} + h^+_{VB}$$

H^- radicals via oxidation. This process leads to the formation of highly reactive oxygen species, such as O_2, $O_2^{\bullet -}$, OH^-, or HOO•, which are crucial for the efficient degradation of organic dyes[60]. To summarize, the reaction proceeds as

$$MgO + h\upsilon \rightarrow e^-_{CB} + h^+_{VB} \tag{8}$$

$$E^-_{CB} + O_2 \rightarrow O_2 \tag{9}$$

$$O_2^{\bullet -} + H^+ \rightarrow HOO \tag{10}$$

$$H_2O + h^+_{VB} \rightarrow OH + H^+ \tag{11}$$

$$HOO^{\bullet} + e^-_{CB} + H^+ \rightarrow H_2O_2 \tag{12}$$

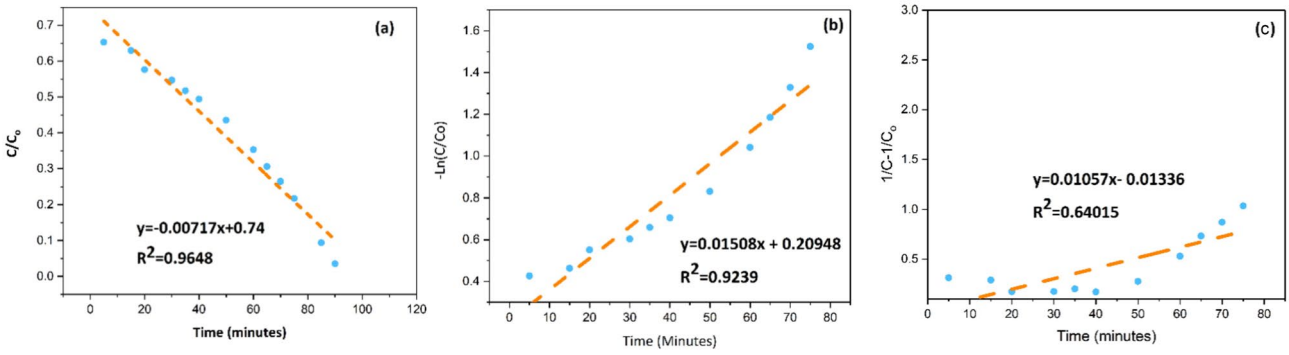

Fig.9. Photodegradation of methylene blue (MB) by MgO nanoparticles under visible light over 110 min, analyzed using kinetic models: (**a**) Zero-order model, (**b**) First-order model, (**c**) Second-order model.

$$H_2O_2 + e_{CB}^- \rightarrow^{\bullet} OH + OH^- \quad (13)$$

CB: Conduction band, VB: Valence band.

The degradation of methylene blue (MB) dye is well-documented to begin with the cleavage of the C–S + , = C bond. This process leads to the complete transformation of nitrogen-containing heteroatoms into ammonium (NH^{4+}), nitrate (NO^{3-}) ions, carbon-containing heteroatoms into carbonate (CO_3^{2-}) ions, and sulfur-containing heteroatoms into sulfate (SO_4^{2-}) ions during the mineralization process[61];

$C_{16}H_{18}N_3S + + 102OH\cdot + \text{visible light} \rightarrow 16CO_2 + 3NO_2^{-3} + SO_2^{-4} + 6H + + 57H_2O$.

The breakdown of MB dye is attributed to the creation of ROS species such as HOO, O_2, OH^-, or $O_2^{\bullet-}$. Moreover, the structural and morphological characteristics of the MgO NPs prepared to play a significant role in the efficiency of the photocatalytic reaction since the reaction occurs on their surface and active sites vary with each morphology. Uniform and well-crystallized MgO NPs can reduce the recombination rate of photogenerated electron–hole pairs, thus promoting rapid photoreactive degradation. The study findings suggest that the prepared MgO nanoparticles exhibit effective photocatalytic activity in degrading organic dyes under UV light exposure. Additionally, the recyclability and photostability of the MgO NPs were assessed by conducting photodegradation experiments under similar conditions, with the MgO NPs washed thrice while being centrifuged following each cycle. The results demonstrate a high level of reusability, with dye degradation rates of 98%, 88%, and 79% achieved during the first, second, and third cycles, respectively[27,62].

Conclusion

This study successfully synthesized MgO nanoparticles using a green chemistry approach, highlighting its environmental friendliness and cost-effectiveness. Extensive characterization techniques, including XRD, FE-SEM, HR-TEM, FTIR, and Raman spectroscopy, were employed to investigate the microstructure and properties of the nanoparticles. XRD analysis confirmed a polycrystalline cubic structure, while FE-SEM images revealed agglomerated quasi-spherical nanoparticle morphology. FTIR analysis verified the presence of Mg-O bonds. The photocatalytic performance of the MgO nanoparticles exhibited an impressive degradation efficiency of 98% for methylene blue dye under visible light within 110 min. These findings demonstrate the potential of MgO nanoparticles as highly effective photocatalysts and adsorbents for treating industrial effluents. Regarding scalability and commercialization, the development of green-synthesized nanoparticles offers a pathway to a more sustainable and resilient future. However, several challenges persist, including the need for precise control over particle characteristics, a deeper understanding of the biosynthesis mechanisms, and ensuring consistent pollutant removal efficiency. The variability in particle sizes and shapes, along with concerns about storage stability, underscores the need for continued refinement of synthesis methods. Additionally, a comprehensive toxicological evaluation and the optimization of genetically modified microorganisms or plants are essential to fully harness the potential of green-synthesized nanoparticles. Despite these challenges, the pursuit of sustainable and efficient nanoscale metal synthesis represents a promising avenue for future scientific research and innovation across disciplines. As progress continues in this field, the potential for greener and more responsible nanoparticle synthesis becomes increasingly apparent.

Data availability

The datasets used and/or analysed during the current study available from the corresponding author on reasonable request.

Received: 31 May 2024; Accepted: 26 August 2024
Published online: 29 August 2024

References

1. Tamboli, S. H. *et al.* Modification of optical properties of MgO thin films by vapour chopping. *J. Alloy. Compd.* **477**(1), 855–859 (2009).
2. Lempicki, A. The electrical conductivity of MgO single crystals at high temperatures. *Proc. Phys. Soc. Sec B* **66**(4), 281–283 (1953).
3. Chanani, J., Buazar, F. & Nikpour, Y. Promoted photocatalytic activity of green titanium oxide-clay nanocomposite toward polychlorinated biphenyl degradation in actual samples. *Water Air Soil Pollut.* **234**(6), 364 (2023).
4. de JesúsRuíz-Baltazar, Á., YobannyReyes-López, S. & de LourdesMondragón-Sánchez, M. Eco-friendly synthesis of Fe3O4 nanoparticles: Evaluation of their catalytic activity in methylene blue degradation by kinetic adsorption models. *Results Phys.* **12**, 989–995 (2019).
5. Kalam, A. *et al.* Modified solvothermal synthesis of cobalt ferrite (CoFe2O4) magnetic nanoparticles photocatalysts for degradation of methylene blue with H2O2/visible light. *Results Phys.* **8**, 1046–1053 (2018).
6. Sagadevan, S. *et al.* Tailoring the structural, morphological, optical, thermal and dielectric characteristics of ZnO nanoparticles using starch as a capping agent. *Results Phys.* **15**, 102543 (2019).
7. Beena, V. *et al.* Enhanced photocatalytic and antibacterial activities of ZnSe nanoparticles. *J. Inorg. Organomet. Polym Mater.* **31**(11), 4390–4401 (2021).
8. Jain, A. *et al.* Colorimetric sensing of Fe3+ ions in aqueous solution using magnesium oxide nanoparticles synthesized using green approach. *Chem. Phys. Lett.* **706**, 53–61 (2018).
9. Ramanujam, K. & Sundrarajan, M. Antibacterial effects of biosynthesized MgO nanoparticles using ethanolic fruit extract of Emblica officinalis. *J. Photochem. Photobiol. B* **141**, 296–300 (2014).
10. Mangalampalli, B., Dumala, N. & Grover, P. Allium cepa root tip assay in assessment of toxicity of magnesium oxide nanoparticles and microparticles. *J. Environ. Sci.* **66**, 125–137 (2018).
11. Salem, J. K. *et al.* Optical and fluorescence properties of MgO nanoparticles in micellar solution of hydroxyethyl laurdimonium chloride. *Chem. Phys. Lett.* **636**, 26–30 (2015).
12. El Bouraie, M. M. & Ibrahim, S. S. Comparative study between metronidazole residues disposal by using adsorption and photodegradation processes onto MgO nanoparticles. *J. Inorg. Organomet. Polym. Mater.* **31**(1), 344–364 (2021).

13. Jorfi, S. *et al.* Enhanced coagulation-photocatalytic treatment of Acid red 73 dye and real textile wastewater using UVA/synthesized MgO nanoparticles. *J. Environ. Manag.* **177**, 111–118 (2016).
14. Karthik, K. *et al.* Fabrication of MgO nanostructures and its efficient photocatalytic, antibacterial and anticancer performance. *J Photochem. Photobiol. B Biol.* **190**, 8–20 (2019).
15. Falyouna, O. *et al.* Synthesis of hybrid magnesium hydroxide/magnesium oxide nanorods [Mg(OH)2/MgO] for prompt and efficient adsorption of ciprofloxacin from aqueous solutions. *J. Clean. Prod.* **342**, 130949 (2022).
16. Yadav, P., Saini, R. & Bhaduri, A. Facile synthesis of MgO nanoparticles for effective degradation of organic dyes. *Environ. Sci. Pollut. Res.* **30**(28), 71439–71453 (2023).
17. Bekhit, S. M. *et al.* Combined effect of adsorption and photocatalytic degradation using magnesium oxide nano-flowers for tetracycline removal. *J. Inorg. Organomet. Polym. Mater.* https://doi.org/10.1007/s10904-024-03138-9 (2024).
18. Camtakan, Z., Erenturk, S. & Yusan, S. Magnesium oxide nanoparticles: Preparation, characterization, and uranium sorption properties. *Environ. Prog. Sustain. Energy* **31**(4), 536–543 (2012).
19. Kumar, A. & Kumar, J. On the synthesis and optical absorption studies of nano-size magnesium oxide powder. *J. Phys. Chem. Solids* **69**(11), 2764–2772 (2008).
20. Shukla, S. K. *et al.* Nano-like magnesium oxide films and its significance in optical fiber humidity sensor. *Sens. Actuators B: Chem.* **98**(1), 5–11 (2004).
21. Zhao, Z. *et al.* Solvo- or hydrothermal fabrication and excellent carbon dioxide adsorption behaviors of magnesium oxides with multiple morphologies and porous structures. *Mater. Chem. Phys.* **128**(3), 348–356 (2011).
22. Umaralikhan, L. Green synthesis of MgO nanoparticles and it antibacterial activity. *Iran. J. Sci. Technol. Trans. A Sci.* **42**(2), 477–485 (2018).
23. Rahimi, S., Buazar, F. & Larki, A. Efficient absorption and sensing of Haloacetonitriles on fullerene C20 surface at DFT level. *Water Air Soil Pollut.* **234**(7), 409 (2023).
24. Fazli, S., Buazar, F. & Matroudi, A. Theoretical insights into benzophenone pollutants removal from aqueous solutions using graphene oxide nanosheets. *Theor. Chem. Acc.* **142**(12), 134 (2023).
25. Khalafi, T., Buazar, F. & Ghanemi, K. Phycosynthesis and enhanced photocatalytic activity of zinc oxide nanoparticles toward organosulfur pollutants. *Sci. Rep.* **9**(1), 6866 (2019).
26. Buazar, F. *et al.* Potato extract as reducing agent and stabiliser in a facile green one-step synthesis of ZnO nanoparticles. *J. Exp. Nanosci.* **11**(3), 175–184 (2016).
27. Buazar, F., Sayahi, M. H. & Zarei Sefiddashti, A. Marine carrageenan-based NiO nanocatalyst in solvent-free synthesis of polyhydroquinoline derivatives. *Appl. Organomet. Chem.* **37**(9), e7191 (2023).
28. Sepahvand, M., Buazar, F. & Sayahi, M. H. Novel marine-based gold nanocatalyst in solvent-free synthesis of polyhydroquinoline derivatives: Green and sustainable protocol. *Appl. Organomet. Chem.* **34**(12), e6000 (2020).
29. Hano, C. & Abbasi, B. H. Plant-based green synthesis of nanoparticles: Production, characterization and applications. *Biomolecules* https://doi.org/10.3390/biom12010031 (2022).
30. Adil, S. F. *et al.* Biogenic synthesis of metallic nanoparticles and prospects toward green chemistry. *Dalton Trans.* **44**(21), 9709–9717 (2015).
31. Noha, A. K. *et al.* Renin and angiotensin converting enzyme inhibition of standardized bioactive fractions of *Hyphaene thebaica* L mart growing in Egypt. *Pharm. J.* **10**(4), 622 (2018).
32. Hkiri, K. *et al.* Biosynthesis and characterization of CaZrO3 nanoparticles *via hyphaene thebaica*: Effect of preparation method on morphology, electrical, and dielectric properties. *J. Mater. Sci. Mater. Electron.* **31**(13), 10018–10030 (2020).
33. Mohamed, H. E. A. *et al.* Bio-redox potential of *Hyphaene thebaica* in bio-fabrication of ultrafine Maghemite phase iron oxide nanoparticles (Fe2O3 NPs) for therapeutic applications. *Mater. Sci. Eng. C* **112**, 110890 (2020).
34. Mohamed, H. E. A. *et al.* Phytosynthesis of BiVO(4) nanorods using *Hyphaene thebaica* for diverse biomedical applications. *AMB Exp.* **9**(1), 200 (2019).
35. Mohamed, H. E. A., Thema, T. & Dhlamini, M. S. Green synthesis of CuO nanoparticles via *Hyphaene thebaica* extract and their optical properties. *Mater. Today Proc.* **36**, 591–594 (2021).
36. Sone, B. T. *et al.* Green-synthesized ZnO via *Hyphaene thebaica* fruit extracts: Structure & catalytic effect on the Ozonation of Coralene Rubine-S2G azo disperse dye. *Environ. Nanotechnol. Monit. Manag.* **16**, 100515 (2021).
37. Mohamed, H. E. A. *et al.* Biosynthesis of silver nanoparticles from *Hyphaene thebaica* fruits and their in vitro Pharmacognostic potential. *Mater. Res. Exp.* **6**(10), 1050c9 (2019).
38. Zhang, H., Chen, G. & Bahnemann, D. W. Photoelectrocatalytic materials for environmental applications. *J. Mater. Chem.* **19**(29), 5089–5121 (2009).
39. Sarojini, P. *et al.* Design of V2O5 blocks decorated with garlic peel biochar nanoparticles: A sustainable catalyst for the degradation of methyl orange and its antioxidant activity. *Materials* https://doi.org/10.3390/ma16175800 (2023).
40. Buazar, F., et al., Biofabrication of highly pure copper oxide nanoparticles using wheat seed extract and their catalytic activity: A mechanistic approach. 2019. **8**(1): p. 691-702.
41. Pugazhendhi, A. *et al.* Anticancer, antimicrobial and photocatalytic activities of green synthesized magnesium oxide nanoparticles (MgONPs) using aqueous extract of Sargassum wightii. *J. Photochem. Photobiol. B: Biol.* **190**, 86–97 (2019).
42. Dekermenjian, M., Ruediger, A. P. & Merlen, A. Raman spectroscopy investigation of magnesium oxide nanoparticles. *RSC Adv.* **13**(38), 26683–26689 (2023).
43. Hassan, S. E. *et al. Rhizopus oryzae*-Mediated green synthesis of magnesium oxide nanoparticles (MgO-NPs): A promising tool for antimicrobial, Mosquitocidal action, and tanning effluent treatment. *J. Fungi* https://doi.org/10.3390/jof7050372 (2021).
44. Dobrucka, R. Synthesis of MgO nanoparticles using *Artemisia abrotanum* Herba Extract and their antioxidant and photocatalytic properties. *Iran. J. Sci. Technol.Trans. A Sci.* **42**(2), 547–555 (2018).
45. Aswal, D. K. *et al.* XPS and AFM investigations of annealing induced surface modifications of MgO single crystals. *J. Cryst. Growth* **236**(4), 661–666 (2002).
46. Awaji, T. *et al.* Improved surface crystallinity of MgO crystal substrate through annealing in oxygen atmosphere. *Jpn. J. Appl. Phys.* **31**(5B), L642 (1992).
47. Geler-Kremer, J., Posadas, A. B. & Demkov, A. A. Preparation of clean MgO surface by oxygen plasma: Comparison with standard substrate cleaning procedures. *J. Vac. Sci. Technol. B* **38**(6), 062201 (2020).
48. Alavi, M. A. & Morsali, A. Syntheses and characterization of Mg(OH)2 and MgO nanostructures by ultrasonic method. *Ultrason. Sonochem.* **17**(2), 441–446 (2010).
49. Akram, M. W. *et al.* In vitro evaluation of the toxic effects of MgO nanostructure in Hela cell line. *Sci. Rep.* **8**(1), 4576 (2018).
50. Athar, T., Deshmukh, A. & Ahmed, W. Synthesis of MgO Nanopowder viaNon aqueous Sol-Gel method. *Adv. Sci. Lett.* **5**, 1–3 (2012).
51. Hema, M. Synthesis of hierarchical structured MgO by sol-gel method. *Nano bull.* **2**, 130106-1–130106 (2013).
52. Rezaei, M., Khajenoori, M. & Nematollahi, B. Synthesis of high surface area nanocrystalline MgO by pluronic P123 triblock copolymer surfactant. *Powder Technol.* **205**(1), 112–116 (2011).
53. Makarov, V. V. *et al.* "Green" nanotechnologies: Synthesis of metal nanoparticles using plants. *Acta Naturae* **6**(1), 35–44 (2014).
54. Koopi, H. & Buazar, F. A novel one-pot biosynthesis of pure alpha aluminum oxide nanoparticles using the macroalgae *Sargassum ilicifolium*: A green marine approach. *Ceram. Int.* **44**(8), 8940–8945 (2018).

55. Moavi, J., Buazar, F. & Sayahi, M. H. Algal magnetic nickel oxide nanocatalyst in accelerated synthesis of pyridopyrimidine derivatives. *Sci. Rep.* **11**(1), 6296 (2021).
56. Buazar, F. *et al.* Facile one-pot phytosynthesis of magnetic nanoparticles using potato extract and their catalytic activity. *Starch-Stärke* **68**(7–8), 796–804 (2016).
57. Jeevanandam, J., Chan, Y. S. & Danquah, M. K. Biosynthesis and characterization of MgO nanoparticles from plant extracts via induced molecular nucleation. *N. J. Chem.* **41**(7), 2800–2814 (2017).
58. Safdar, A. *et al.* Green synthesis of cobalt oxide nanoparticles Using *Hyphaene thebaica* fruit extract and their photocatalytic application. *Appl. Sci.* https://doi.org/10.3390/app13169082 (2023).
59. Singh, J., et al., *Biogenic ZnO nanoparticles: a study of blueshift of optical band gap and photocatalytic degradation of reactive yellow 186 dye under direct sunlight.* **8**(1): 272–280. (2019).
60. Rahman, Q. I. *et al.* Effective photocatalytic degradation of rhodamine B dye by ZnO nanoparticles. *Mater. Lett.* **91**, 170–174 (2013).
61. Kumar, S. A. *et al.* Facile green synthesis of magnesium oxide nanoparticles using tea (Camellia sinensis) extract for efficient photocatalytic degradation of methylene blue dye. *Environ. Technol. Innov.* **28**, 102746 (2022).
62. Torfi-Zadegan, S., Buazar, F. & Sayahi, M. H. Accelerated sonosynthesis of chromeno[4,3-b]quinoline derivatives via marine-bioinspired tin oxide nanocatalyst. *Appl. Organomet. Chem.* **37**(12), e7286 (2023).
63. Nijalingappa, T. B. *et al.* Antimicrobial properties of green synthesis of MgO micro architectures via *Limonia acidissima* fruit extract. *Biocatal. Agric. Biotechnol.* **18**, 100991 (2019).
64. Mirzaei, H. & Davoodnia, A. Microwave assisted sol-gel synthesis of MgO nanoparticles and their catalytic activity in the synthesis of Hantzsch 1,4-dihydropyridines. *Chin. J. Catal.* **33**(9), 1502–1507 (2012).
65. Mohanasrinivasan, V. *et al.* Biosynthesis of MgO nanoparticles using lactobacillus Sp. and its activity against human Leukemia cell lines HL-60. *BioNanoScience* **8**(1), 249–253 (2018).
66. Kumar, S. *et al.* Facile synthesis of hierarchical Cu2O nanocubes as visible light photocatalysts. *Appl. Catal. B Environ.* **189**, 226–232 (2016).
67. Zou, W. *et al.* Engineering the Cu2O-reduced graphene oxide interface to enhance photocatalytic degradation of organic pollutants under visible light. *Appl. Catal. B Environ.* **181**, 495–503 (2016).
68. Nezamzadeh-Ejhieh, A. & Karimi-Shamsabadi, M. Decolorization of a binary azo dyes mixture using CuO incorporated nanozeolite-X as a heterogeneous catalyst and solar irradiation. *Chem. Eng. J.* **228**, 631–641 (2013).
69. Lamba, R. *et al.* Well-crystalline porous ZnO–SnO2 nanosheets: An effective visible-light driven photocatalyst and highly sensitive smart sensor material. *Talanta* **131**, 490–498 (2015).
70. Prasad, N. & Balasubramanian, K. Optical, phonon and efficient visible and infrared photocatalytic activity of Cu doped ZnS micro crystals. *Spectrochim. Acta Part A Mol. Biomol. Spectrosc.* **173**, 687–694 (2017).
71. Yousefi, R. *et al.* Enhanced visible-light photocatalytic activity of strontium-doped zinc oxide nanoparticles. *Mater. Sci. Semicond. Proc.* **32**, 152–159 (2015).
72. Azarang, M. *et al.* One-pot sol–gel synthesis of reduced graphene oxide uniformly decorated zinc oxide nanoparticles in starch environment for highly efficient photodegradation of Methylene Blue. *RSC Adv.* **5**(28), 21888–21896 (2015).

Author contributions

AM and HEAM conceptualization of the research. AM, AS, KH, HEAM, LK and MM performed facilitation for material characterization and analyze the results. AM,AS, and HEAM prepared 1st draft of the paper. AM, ASKH, HEAM, SA and MM reviewed and improved the manuscript. All authors agree to submit the paper.

Competing interests

The authors declare no competing interests.

Additional information

Correspondence and requests for materials should be addressed to H.E.A.M.

Reprints and permissions information is available at www.nature.com/reprints.

Publisher's note Springer Nature remains neutral with regard to jurisdictional claims in published maps and institutional affiliations.